



## Microstructural investigation and castability anticipation in modern Ti/Al/Nb-containing nickel-based superalloys

Homam NAFFAKH-MOOSAVY

Department of Materials Engineering, Faculty of Engineering,  
Tarbiat Modares University, P. O. Box 14115-143, Tehran, Iran

Received 11 July 2015; accepted 2 March 2016

**Abstract:** A quantitative relation between the  $\gamma/\gamma'$  and  $\gamma/\text{Laves}$  intermetallics was investigated with the change of chemical composition, i.e., Ti, Al and Nb in the third generation of nickel-based superalloys. The results demonstrated that the maximum amount of intermetallic eutectics (i.e., 41.5%, mass fraction) has been formed in 9.8% (Ti+Al). It is predicted that high level of intermetallics formed in the 3GSA-HNM-1 ( $\gamma$ -9.8%(Ti+Al)) deteriorates its castability. The type and morphology of eutectic intermetallics change and the amount considerably diminishes by decreasing Ti+Al in 3GSA-HNM-2 ( $\gamma$ -7.6%(Ti+Al), 1.5% Nb). Thus, it is predicted that the castability for the 3GSA-HNM-2 improves. The amount of Laves intermetallics shows an ascending behavior again, however, with less intensity by increasing the Nb content in the 3GSA-HNM-3 ( $\gamma$ -5.7%(Ti+Al), 2.9% Nb). It can be concluded that for 3GSA-HNM-3 with composition of  $\gamma$ -5.7%(Ti+Al) and 2.9% Nb, the optimized castability can be anticipated, because the minimum amount of eutectic intermetallics (i.e., 4.7%) is formed.

**Key words:** nickel-based super alloys; secondary phases; castability; segregation; microstructure

### 1 Introduction

The combination of high strength and excellent corrosion resistance makes the precipitation-strengthened Ni-based superalloys unique among high-performance alloy systems [1,2]. The first generation of precipitation-strengthened Ni-based superalloys contains titanium and aluminum that form strengthening precipitates with nickel after an appropriate heat treatment. The most common of these precipitates are called gamma prime ( $\gamma'$ -Ni<sub>3</sub>Al, Ni<sub>3</sub>Ti, and Ni<sub>3</sub>(Ti,Al)) [3–6]. The second generation of superalloys shows slow aging response of  $\gamma''$ -Ni<sub>3</sub>Nb which makes these alloys essentially immune to strain-age cracking. The third generation of nickel-based superalloys contains the  $\gamma'$ - and  $\gamma''$ -former elements such as Ti, Al and Nb simultaneously [1,2,7]. Although the  $\gamma'$  and  $\gamma''$  intermetallic compounds are formed within the austenite matrix by heat treatment, casting and fusion welding of these superalloys face serious challenges from castability and weldability viewpoints. The castability and weldability are strongly the function of type, distribution, amount and morphology of the intermetallics, which are formed in the microstructures

of superalloy [8–11]. Significant investigations have been carried out on intermetallic precipitates in the first generation of nickel-based superalloys which exhibit that Al and Ti form intermetallic eutectics within the grain boundaries and interdendritic regions, which can severely decrease the castability and weldability of the superalloys [3–5,12–15]. The observations demonstrate that Al and Ti form cluster  $\gamma/\gamma'$  intermetallic eutectics in the grain boundaries and interdendritic regions, which causes the solidification temperature range to increase. The widening of solidification temperature range can sensitize the superalloys to the solidification cracking. Indeed, the eutectic intermetallic constituents provide the locations for the crack nucleation and growth [2,12–15]. Considerable studies have been conducted on the correlations between the intermetallics and castability and weldability of the second generation of nickel-based superalloys [16–30].

Although the niobium is necessary for nucleation and formation of  $\gamma''$  intermetallic precipitates in the nickel austenite, Nb can promote the formation of  $\gamma/\text{Laves}$  intermetallic eutectics during the final stage of solidification of molten superalloys. This eutectic phase may lead to challenges similar to which happens in the

first generation superalloys [2,16,18,27]. The researches display that  $\gamma$ /Laves intermetallic eutectics decrease the solidus temperature and widen the brittleness temperature range (BTR). In other words, the solidification cracking has increased, when the BTR of superalloys widens. Furthermore, it is interpreted that the accumulation of continuous  $\gamma$ /Laves intermetallic eutectics within the grain boundaries and interdendritic regions induces a more destructive effect on the hot cracking in comparison to discontinuous eutectics. In addition, the globular  $\gamma$ /Laves intermetallic eutectics exhibit less potential for crack nucleation and propagation than irregular  $\gamma$ /Laves intermetallic eutectics [17,19,25]. In spite of studies performed on the third generation of nickel-based superalloys which contain Ti, Al and Nb simultaneously, the correlation among type, amount, morphology and distribution of intermetallic compounds has not been properly and sufficiently investigated. Therefore, the target of the present study is to make rational and quantitative relation between the type, amount, morphology and distribution of  $\gamma/\gamma'$  and  $\gamma$ /Laves intermetallic eutectic compounds with the change of chemical composition, i.e., Ti, Al and Nb in the third generation of nickel-based superalloys. Finally, the research attempts to introduce an optimized microstructure, in which the minimum amount of  $\gamma/\gamma'$  and  $\gamma$ /Laves intermetallic eutectic compounds is formed; therefore, the best castability for the current compositions is anticipated.

## 2 Experimental

Four new superalloys were designed. The amount of Ti+Al decreased from 9.8% in Alloy 1 to 3.7% in Alloy 4 as a variable parameter. Contrariwise, the amount of Nb increased from 0 in Alloy 1 to 4.4% in Alloy 4. The chemical compositions of the newly-designed superalloys are listed in Table 1. The composition analyses were performed by appropriate techniques after completion of each relevant making processes. It is necessary to say that the amount of impurities has been accurately measured, and it has been tried to keep the amount of C, N, P+S fixed and less than 0.05%, ~0.005%, 0.005%, respectively. Further, the casting operation was done by a fully-vacuumed vacuum induction melting (VIM) during the both melting and pouring operations to avoid any absorption of air nitrogen. The VIM furnace with vacuum capacity of  $10^{-4}$  bar, the frequency of 3.6 kHz and the maximum power of 60 kW was employed for melting of the metallic elements and adjusting the designed composition of superalloys. Pure alumina crucible with 1000 mL volume, and steel die with dimensions of 150 mm  $\times$  100 mm  $\times$  50 mm were employed for pouring

the resultant molten alloys. The temperature of 1450 °C was selected for full melting of the alloys. The ingots were cooled at the ambient temperature. The specimens were cut by wire to the desired dimensions and then were sent to metallography lab for final microstructural characterization. After the casting operations, abrasive cutting and cleaning, the specimens were prepared according to the standard metallographic procedures. Marble etching solution (5 g CuSO<sub>4</sub> + 100 mL H<sub>2</sub>O + 100 mL HCl) was used to reveal the microstructures. After the metallographic preparations, the identification of the intermetallic type, amount, size, morphology and distribution was carried out by Leitz Wetzlar Aristomet optical microscope equipped with Nikon ACT Version 2.70 image analyzer software. Further microstructural investigations were performed by a Zeiss EVO 50XVP scanning electron microscope (SEM) in secondary electron (SE) and back scattered electron (BSE) with accelerating voltage of 30 kV equipped with an Oxford Instrument 7060 energy dispersive X-ray spectrometer (EDS) having INCA quantitative analysis program for spot, line and map mass analysis. The quantitative measurements of secondary phases, i.e., intermetallic eutectics was accomplished by Image Analyzer Pro. Plus 4.5 version 2001.

**Table 1** Chemical compositions of newly-designed superalloys (mass fraction, %)

Alloy	Ni	Cr	Co	Fe	Mo	Al	Ti	Nb
3GSA-HNM-1	52.7	19	14.8	–	3.5	3	7	–
3GSA-HNM-2	52.4	19	11.1	4.6	3.5	2.4	5.5	1.5
3GSA-HNM-3	52	19	7.4	9.4	3.5	1.8	4	2.9
3GSA-HNM-4	51.8	19	3.7	13.9	3.5	1.2	2.5	4.4

## 3 Results and discussion

### 3.1 Intermetallics and secondary phases in microstructure of 3GSA-HNM-1

Figures 1(a)–(d) show full set of low magnification optical microstructures used for phase measurements in the new superalloys. Also, an instance result of Image Analyzer software is presented in Fig. 1(e). The microstructure of 3GSA-HNM-1 with the composition of  $\gamma$ -9.8%(Ti+Al) is shown in Fig. 2. The overall and dendritic core chemical compositions of 3GSA-HNM-1 are presented in Table 2. Also, the EDS spot microanalysis of the secondary phases is exhibited in Figs. 2(c–f). The compositions of the related intermetallics and secondary phases are collected in Table 2. The type, quantitative amount, morphology and distribution of the secondary phases within the 3GSA-HNM-1 microstructure are shown in Table 3.

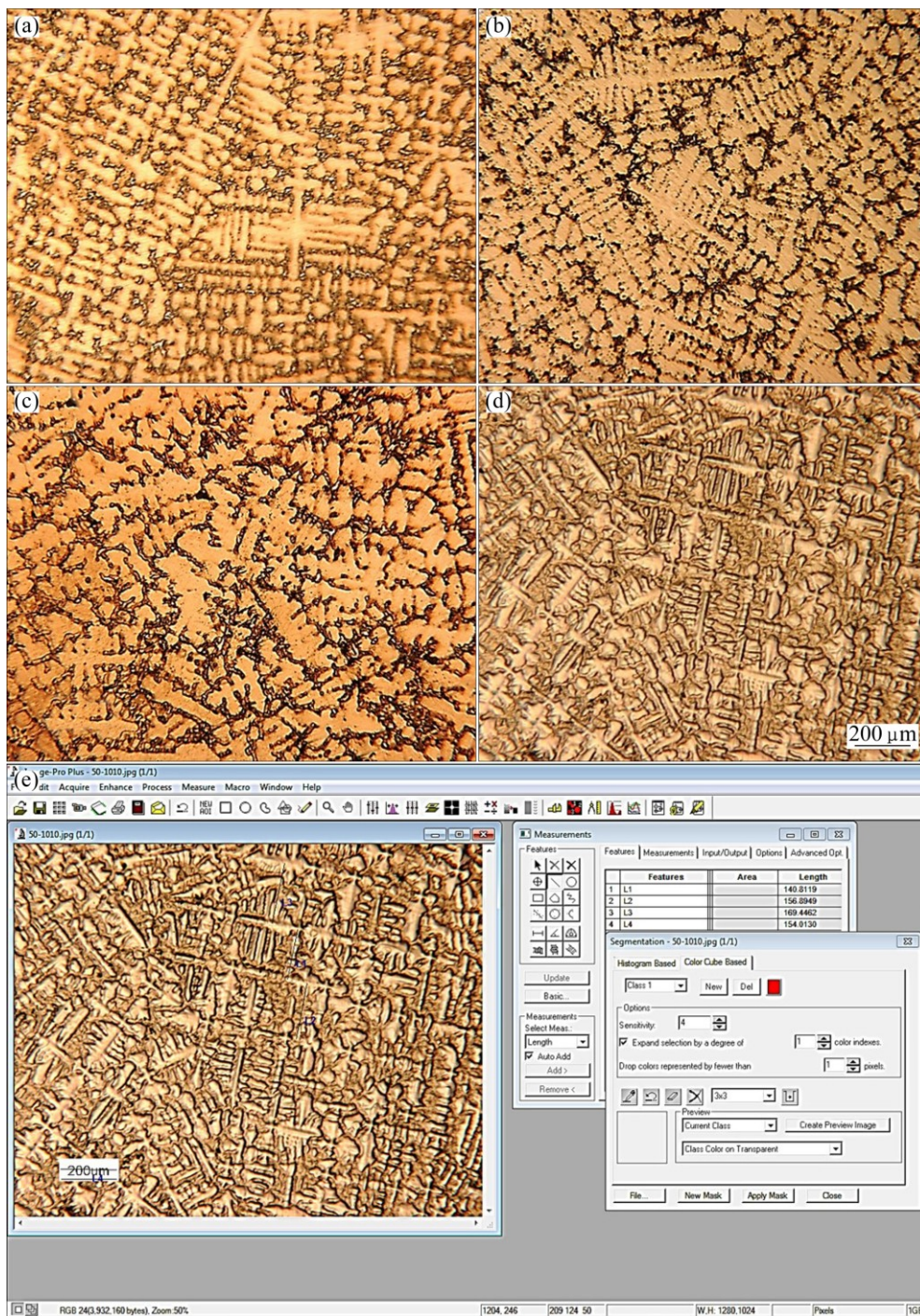


**Fig. 1** A full set of low magnification optical microstructures used for phase measurements: (a) Microstructure of 3GSA-HNM-1; (b) Microstructure of 3GSA-HNM-2; (c) Microstructure of 3GSA-HNM-3; (d) Microstructure of 3GSA-HNM-4; (e) A result of image analyzer software

Figure 2 illustrates several types of precipitates, secondary phases and intermetallic eutectics at different magnifications. According to Fig. 2(a), it can be said that the as-cast microstructure is fully columnar dendritic and the austenitic primary and secondary arms have completely grown. The dendritic cores are seen shiny and the interdendritic regions containing the secondary phases and the eutectic intermetallics have been

identified by a darker color. The eutectics and some voids are observed more clearly in Fig. 2(a).

Figures 2(b) and (c) show dispersed and coarse precipitates with cuboidal morphology and black color labeled “A” on the figure. Based on the results mentioned in Figs. 2(c–f) and Table 2, these precipitates are enriched in Ti and Al; therefore, these can be (Al,Ti)(CN) complex carbonitrides, which are formed during the

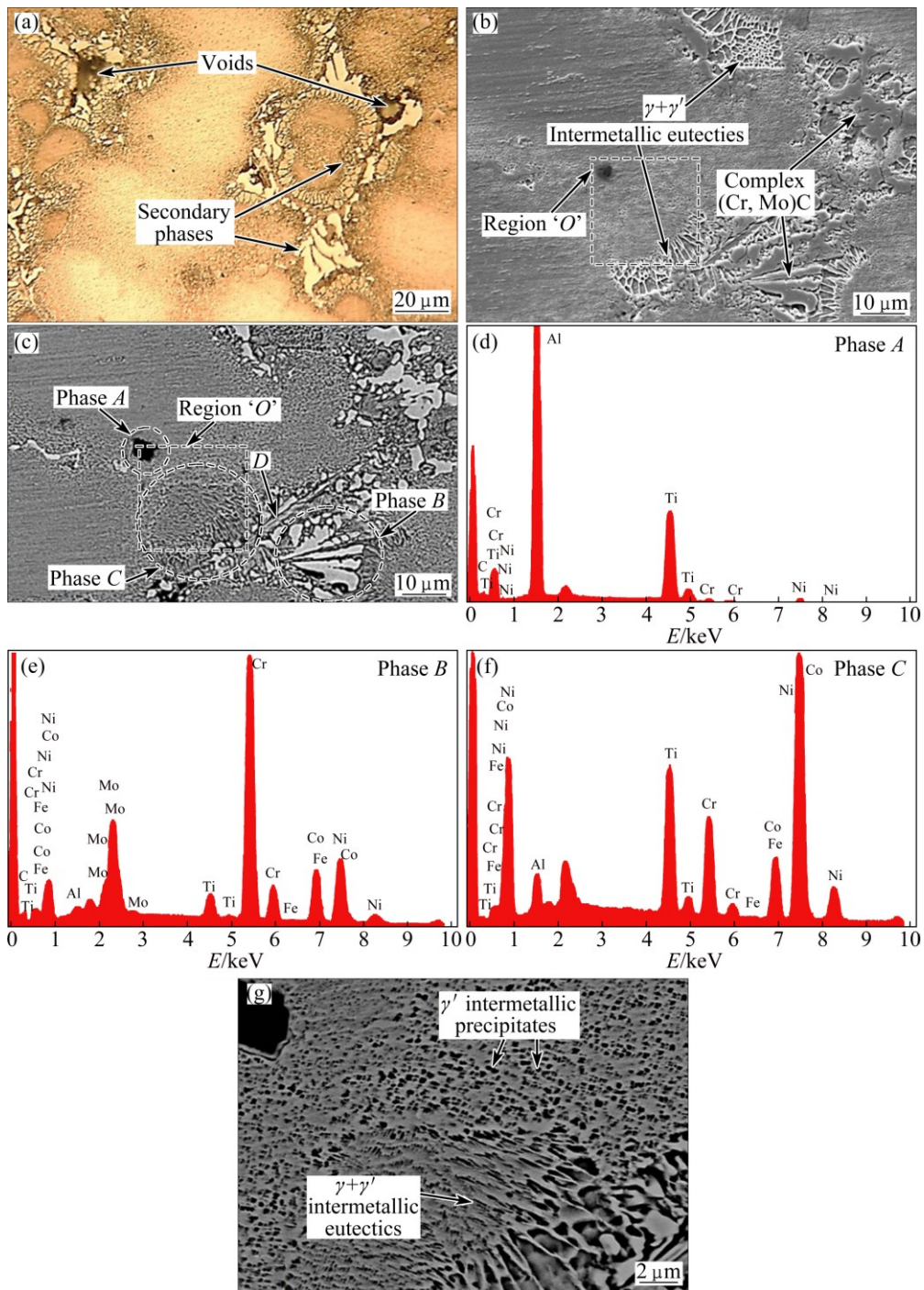


**Fig. 2** Microstructures and EDS analyses of 3GSA-HNM-1: (a) Secondary phases and shrinkage voids in interdendritic regions; (b) SEM image showing distribution of secondary phases in interdendritic regions in SE mode; (c) BSE mode of Fig. 2(b); (d, e, f) EDS microanalysis of secondary phases; (g) Enlarged region 'O' from Figs. 2(b) and (c) showing morphology and distribution of intermetallic compounds and eutectics within boundaries in BSE mode

cooling of superalloy. In fact, the formation of such constituents has been reported for the superalloys containing high Ti+Al contents [31,32]. The presence of this phase in the interdendritic locations exhibits that segregating C and Ti in the interdendritic liquid is the factor causing the formation of complex carbonitrides. In Region "B" white lamellar structures are seen in

Fig. 2(c). According to Figs. 2(c–f) and Table 2, they are rich in Cr and Mo, which are formed in the interdendritic places. It is eutectic structure as complex  $\gamma+(\text{Cr, Mo})_x\text{C}_y$ , in which  $\gamma$  is austenite. Some investigations have clarified that it can nucleate directly from the molten alloy and form as  $\gamma+\text{MC}$  in the interdendritic regions. Thus, the molten interdendritic regions solidify as the

**Table 2** Chemical analysis of dendritic cores and secondary phases in microstructure of 3GSA-HNM-1 (mass fraction, %)

Item	Ni	Co	Cr	Fe	Mo	Nb	Ti	Al
Alloy composition	52.4	14.7	19.6	–	3.5	–	7.1	2.7
Dendrite core	53.7	16	19.6	–	3.3	–	4.7	2.7
Phase A	–	–	–	–	–	–	45	55
Phase B	21.2	14.8	45	–	15	–	3	1
Phase C	61.6	12.4	10.9	–	–	–	12.1	3

**Table 3** Type, morphology, distribution of secondary phases and intermetallic eutectics in 3GSA-HNM-1 microstructure

No.	Phase transformation	Phase amount (surface)	Morphology	Distribution
1	$L$	Remained	Austenitic dendrites	All microstructures
2	$\gamma \rightarrow$ (Al, Ti)(CN)	>1%	Cuboidal precipitates	Interdendritic regions
3	$L \rightarrow$ $\eta$ -Ni-Ti	Unknown	Planar Intermetallics	Interdendritic regions
4	$L \rightarrow \gamma +$ $\text{Ni}_3(\text{Ti}, \text{Al})$	37.2%	Lamellar intermetallic eutectics	Interdendritic regions
5	$L \rightarrow \gamma +$ (Cr, Mo) <sub>x</sub> C <sub>y</sub>	4.3%	Lamellar eutectics	Interdendritic regions
6	$\gamma \rightarrow$ $\text{Ni}_3(\text{Ti}, \text{Al}); \gamma'$	Unmeasurable	Nano-cuboidal precipitates	Interdendritic regions

following reactions:



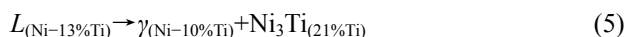
Secondary phases in Eq. (2) refer to phases beyond the austenite (i.e., the primary phase formed), which are formed after the formation of austenite matrix. According to Fig. 2(g), significant areas of the interdendritic regions are occupied by nanometric strengthening intermetallics with the composition of  $\gamma'$ -Ni<sub>3</sub>(Ti,Al). It is noteworthy that such precipitates have not been formed within the dendrite cores. The segregation of Ti in the spaces between the dendrites (i.e., interdendritic locations) during the solidification process promotes the formation of  $\gamma'$  intermetallic compounds. This phenomenon is observed in superalloys containing Ti+Al more than 6% [33,34].

Another layered structure can be identified in the vicinity of  $\gamma'$  precipitates, which is labeled by “C” in Fig. 2(c). This structure contains more Ti (i.e., 12.1%) in comparison to the austenite matrix (i.e., 4.7%) (see Table 2 and Fig. 2(c)). The darker color of this structure than the matrix in BSE mode shows the presence of Ti and Al light elements. Therefore, it can be interpreted that it is

$\gamma + \text{Ni}_3(\text{Ti}, \text{Al})$  intermetallic eutectics called  $\gamma + \gamma'$ . The eutectic formation follows the following phase reaction:



Reaction (4) follows the eutectic reaction in the Ni-Ti-C ternary equilibrium system. The equilibrium eutectic reaction in this system is as follows:



The phase “D” is formed in the vicinity of  $\gamma + \text{Ni}_3(\text{Ti}, \text{Al})$  intermetallic eutectics, which is observed in Fig. 2(c). The phase is too small to be characterized by EDS. It may be an eta ( $\eta$ ) Ni-Ti intermetallic phase, which has been referred to in an earlier study [35].

Quantitative measurements by related software demonstrated that a significant amount (i.e., 37.2%) of  $\gamma + \gamma'$  intermetallic eutectic has been formed in the interdendritic regions (Fig. 1(a)). Also,  $\gamma + (\text{Cr}, \text{Mo})_x\text{C}_y$  has occupied about 4.3% of the interdendritic regions. The amount of (Al,Ti)(CN) and  $\gamma + \gamma'$  phases are predicted to be less than 1%. The summary of type, amount, morphology and distribution of secondary phases and intermetallic eutectics is presented in Table 3.

### 3.2 Intermetallics and secondary phases in microstructure of 3GSA-HNM-2

Figure 3 illustrates the microstructure and secondary phase distribution of 3GSA-HNM-2 with the composition of  $\gamma$ -7.6%(Ti+Al) and 1.5% Nb. The total and dendritic core chemical compositions of the 3GSA-HNM-2 are presented in Table 4. Also, the EDS spot microanalysis of the secondary phases is exhibited in Figs. 3(c,d,e). The compositions of the related intermetallics and secondary phases are collected in Table 4. The type, amount, morphology and distribution of the secondary phases within the 3GSA-HNM-2 microstructure are shown in Table 5.

Figure 3(a) shows the dendritic microstructure of 3GSA-HNM-2. It indicates that secondary phases and precipitates are formed in the interdendritic regions. In addition, some shrinkage porosities are formed in the microstructure. It is interesting to say that the interior of the austenite dendrites has experienced a significant precipitation in itself. It appears that such precipitates are formed after completion of the solidification process during the cooling of the solidified alloy.

**Table 4** Chemical analysis of dendritic cores and secondary phases in microstructure of 3GSA-HNM-2 (mass fraction, %)

Item	Ni	Co	Cr	Fe	Mo	Nb	Ti	Al
Alloy composition	52	11.3	19	5.1	3.5	1.5	5.5	2.1
Dendrite core	53.6	12.3	19.5	5.4	3	0.5	3.7	2
Phase A	38	9.5	16	3.3	10.3	11.5	10.6	0.8
Phase B	1.6	1	1.2	0.2	5.3	40.5	50	0.2

**Table 5** Type, amount, morphology, distribution of secondary phases and intermetallic eutectics in 3GSA-HNM-2 microstructure

No.	Phase transformation	Phase amount (surface)	Morphology	Distribution
1	$L \rightarrow \gamma$	Remained	Austenitic dendrites	All microstructures
2	$\gamma \rightarrow \text{TiC} \rightarrow (\text{Ti, Nb})\text{C}$	3%	Cuboidal precipitates	Austenitic dendrites
3	$L \rightarrow \eta\text{-Ni-Ti}$	Unknown	Planar intermetallics	Interdendritic regions
4	$L \rightarrow \gamma + \text{Laves}$	6.1%	Lamellar intermetallic eutectics	Interdendritic regions

Figure 3(b) displays the interdendritic regions by brighter color in comparison to the cores. It can be attributed to the segregation of alloying elements with

large atoms and their participation in the formation of secondary phases at the boundaries. According to Table 4, it can be distinguished that the amount of dendrite core Nb (i.e., 0.5%) is much less than the total Nb content of the alloy (i.e., 1.5%). It indicates that large portion of Nb has been depleted from the dendritic cores and rejected to the interdendritic liquid during the solidification process. This phenomenon can be attributed to the limited solubility of Nb in Ni austenite according to Ni–Nb binary phase diagram. Accordingly, the rejected Nb can form additional phases (i.e., secondary phases such as eutectics) in the interdendritic regions when the composition of Nb in the liquid exceeds the required composition for the formation of secondary phases. Also, some fraction of Nb is consumed in the dendritic core by formation of Nb-containing secondary phases. Ti exhibits a similar manner to Nb from the segregation viewpoint. The amount of Ti decreases from 5.5% in the alloy

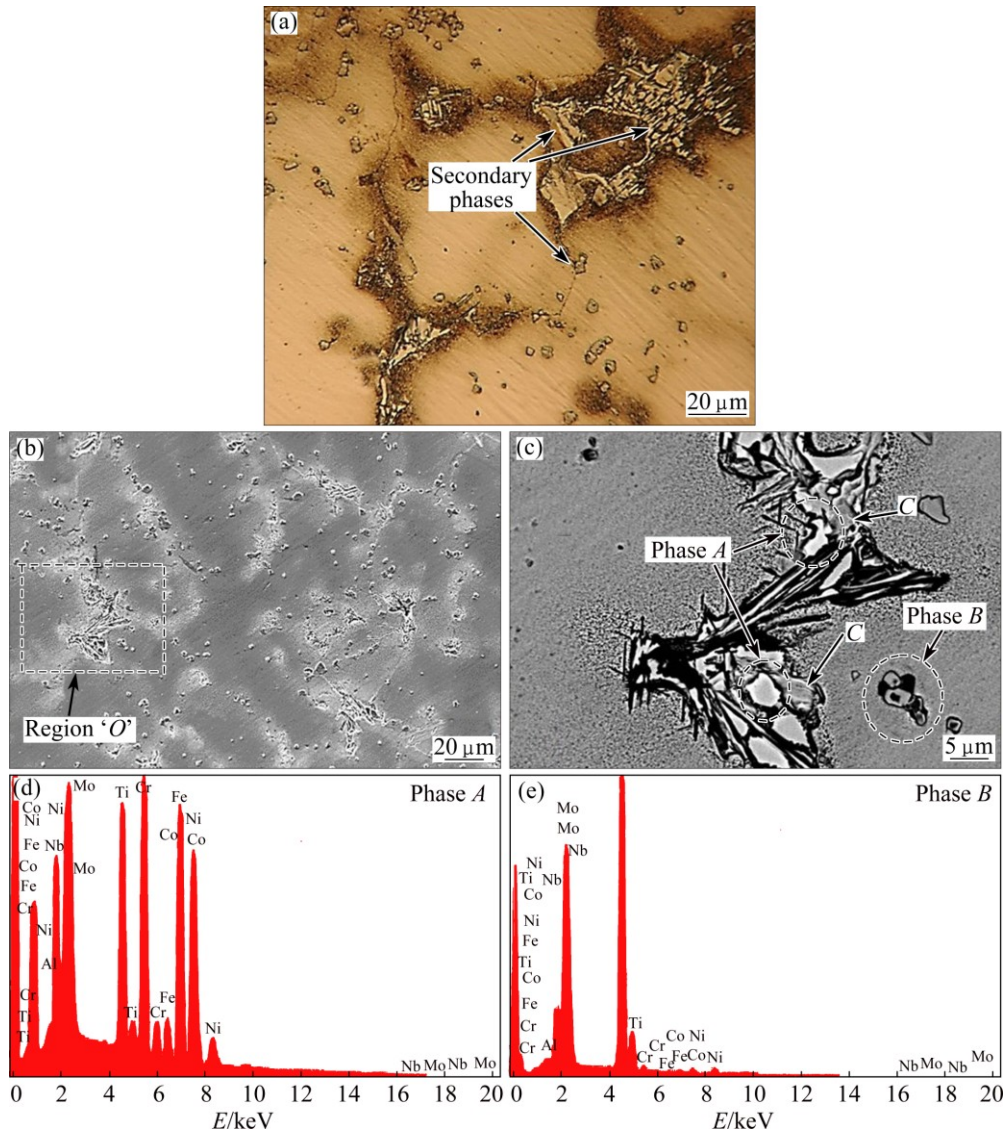


**Fig. 3** Microstructures of 3GSA-HNM-2: (a) Secondary phases in interior and interdendritic regions; (b) Distribution of secondary phases in interior and interdendritic regions in SE-SEM mode; (c) Enlarged region 'O' from Fig. 3(b) showing distribution of secondary phases in interior and interdendritic regions in BSE-SEM mode at higher magnification; (d, e) EDS microanalysis

nominal composition to 3.7% in the dendritic core. Mo and Al have allocated the next rank in the segregation severity. The austenite formers Ni, Cr, Co and Fe represent no considerable segregation. On the basis of Fig. 3(b), several secondary phases are observed within the microstructure. A semilamellar phase with white color is seen in Fig. 3(c), which is specified by “A”. Since this phase has been located in the interdendritic zones, then, it can be interpreted that it has been directly transformed from the retained melt at the last stage of the solidification. It is noteworthy that its color is brighter than that of the matrix in the BSE-SEM mode. It indicates that elements with large atoms, i.e., Nb and Mo participate in the formation of the phase. Figures 3(c, d, e) and Table 4 show that it is enriched in Nb, Mo and Ti. Although the 3GSA-HNM-2, like to 3GSA-HNM-1, contains high level of Ti+Al, however, phase A has no morphological similarity to  $\gamma+\gamma'$  intermetallic eutectic. This phase shows more conformity to  $\gamma$ +Laves intermetallic eutectics, which are formed in the Nb-bearing superalloys. Some studies have reported the formation of such eutectics as  $\gamma+\text{Ni}_3\text{Nb}$  in the Nb-bearing superalloys [2,16]. These investigations clarify that the total amount of Nb, Ti, Mo in Laves intermetallics is in the range of 22%–36%, and the rest elements Ni, Cr, Co, Fe are in the range of 64%–78%. In the 3GSA-HNM-2, the amount of Nb, Ti and Mo is 11.5%, 10.6% and 10.3%, respectively. In this case, the total amount of these elements is 32.4%, which falls within the above mentioned range. So, it can be concluded that phase A is a  $\gamma$ +Laves intermetallic eutectic, in which the Laves is formed as  $(\text{Ni,Cr,Co, Fe})_x(\text{Nb, Ti, Mo})_y$  chemical formula on the basis of  $\text{A}_2\text{B}$  intermetallic compound. It is possible to write the above constituent as  $\gamma+\text{Ni}_2(\text{Nb,Ti,Mo})$ . Therefore, the formation reaction of this phase is given as follows:



Phase reaction (6) follows the eutectic reaction of Nb–Ti–Al ternary equilibrium system as given below:



The formation of this phase shows that the decreasing total amount of Ti+Al from 9.8% to 7.6%, and increasing Nb content from 0 to 1.5% are the governing factors, which substitute the  $\gamma$ +Laves intermetallic eutectic for the  $\gamma+\gamma'$ . On the other hand, relatively coarse precipitates with cubic morphology and dimension of  $\sim 2 \mu\text{m}$  are observed in Figs. 3(b) and (c). According to Fig. 3(c) which is provided in BSE mode, it is identified that the precipitates contain two sections: the external cover and the internal core. The internal core is darker than the external cover. On the basis of EDS measurements (Table 4 and Fig. 3(c)), it is specified that

the core and the outer region of precipitates are enriched in Ti and Nb, respectively. The cubic morphology and its composition indicate the formation of a carbide or a complex Ti–Nb carbonitride as  $(\text{Ti,Nb})(\text{CN})$ . It has been formed as  $(\text{Ti,Al})(\text{CN})$  in the 3GSA-HNM-1 due to the absence of Nb in its composition. The other difference between 3GSA-HNM-1 and -2 is in the percentage of the precipitated carbonitrides. It has been formed more extensively in the 3GSA-HNM-2.

Not only this phase has precipitated in the interdendritic regions, but also the interior of the dendrite cores of 3GSA-HNM-2 has experienced a severe precipitation. The formation of less amount of carbonitrides in the superalloy microstructure is attributed to the consumption of Ti by  $\gamma+\gamma'$  intermetallic eutectic reaction. According to specific morphology of these carbonitrides, it can be interpreted that the primary TiC has been formed in the microstructure before the completion of solidification process. By decreasing the temperature, the NbC constituents have nucleated and precipitated on the TiC particles. It means that the formation temperature of TiC is higher than that of NbC. The phase C is a plate-like eta ( $\eta$ ) Ni–Ti intermetallics, which was also seen in the microstructure of 3GSA-HNM-1. It may be formed directly from the molten alloy. The microstructural characterization made by software showed that  $(\text{Ti,Nb})(\text{CN})$  precipitates have occupied about 3% of the microstructure (Fig. 1(b) and Fig. 3(a)), whereas the amount of intermetallic eutectics is 6.1%, which is several times less than that of the intermetallic eutectics  $\gamma+\gamma'$  formed in the 3GSA-HNM-1 microstructure. The type, morphology, distribution of secondary phases and intermetallic eutectics in the 3GSA-HNM-2 microstructure are summarized in Table 5.

### 3.3 Intermetallics and secondary phases in microstructure of 3GSA-HNM-3

Figure 4 illustrates the microstructure and secondary phase distribution of 3GSA-HNM-3 with composition of  $\gamma$ -5.7%(Ti+Al) and 2.9% Nb. The total and dendritic core chemical compositions of the 3GSA-HNM-3 are presented in Table 6. Also, the EDS spot microanalysis of the secondary phases is exhibited in Fig. 4(c). The compositions of the related intermetallics and secondary phases are collected in Table 6. The type, quantitative amount, morphology and distribution of the secondary phases within the 3GSA-HNM-3 microstructure are shown in Table 7.

Figure 4(a) shows the dendritic structure of 3GSA-HNM-3. Various secondary phases are seen in the interdendritic locations. Some of them have grown by acicular or disk shape from the dendrite boundaries toward inside the dendrite with specific orientations.

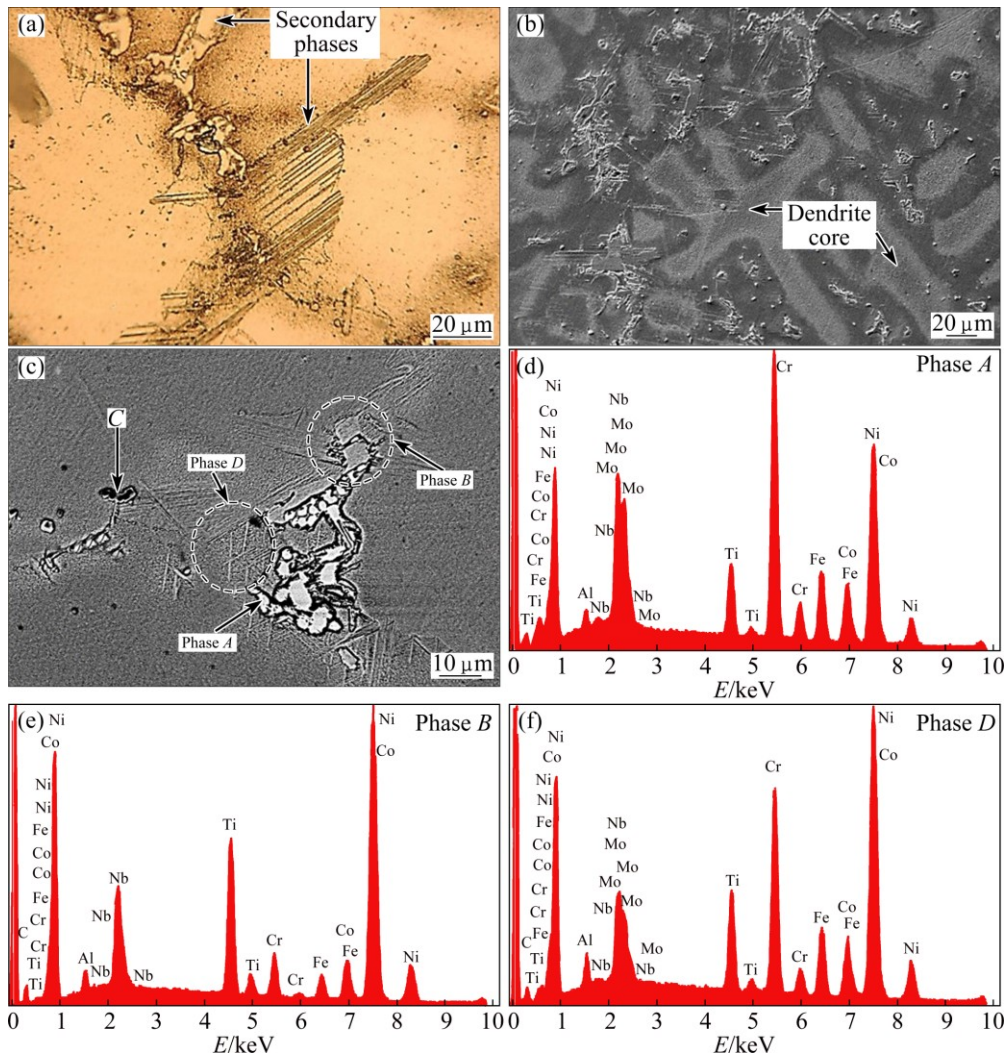


**Fig. 4** Microstructures of 3GSA-HNM-3: (a) Secondary phases in interdendritic regions; (b) Distribution of secondary phases in interdendritic regions in SE mode; (c) Distribution of secondary phases in interdendritic regions in BSE mode at higher magnification; (d, e, f) EDS microanalysis

**Table 6** Chemical analysis of dendritic cores and secondary phases in microstructure of 3GSA-HNM-3 (mass fraction, %)

Item	Ni	Co	Cr	Fe	Mo	Nb	Ti	Al
Alloy composition	52	7.5	19	9.5	3.5	2.8	4	1.7
Dendrite core	53	8.5	20.2	10.3	2.1	1.7	2.7	1.5
Phase A	39.8	8.6	15	6.3	6.7	18	4.6	1
Phase B	56.6	6.6	3.9	2.8	7.9	9.6	11.3	1.3
Phase C	51.4	7.7	15.8	7.3	5	5.6	5.6	1.6
Phase D	52	7.5	19	9.5	3.5	2.8	4	1.7

Furthermore, irregular and lamellar structures with white color can be observed.

A complete dendrite is seen in Fig. 4(b), which is surrounded by the segregants and the secondary phases. White precipitates with lamellar morphology are specified by “A” in Fig. 4(c). Their morphology has a great similarity to that of intermetallic eutectics observed

**Table 7** Type, amount, morphology, distribution of secondary phases and intermetallic eutectics in 3GSA-HNM-3 microstructure

No.	Phase transformation	Phase amount (surface)	Morphology	Distribution
1	$L \rightarrow \gamma$	Remained	Austenitic dendrites	All microstructures
2	$\gamma \rightarrow \text{TiC} \rightarrow (\text{Ti, Nb})\text{C}$	>1%	Cuboidal precipitates	Austenitic dendrites
3	$L \rightarrow \eta\text{-Ni-Ti}$	10.3%	Planar intermetallics	Interdendritic regions
4	$L \rightarrow \gamma + \text{Laves}$	4.7%	Lamellar intermetallic eutectics	Interdendritic regions
5	$\gamma \rightarrow \text{Ni}_3\text{Nb}:\delta$	Unmeasurable	Needle-like precipitates	Interdendritic regions

in the 3GSA-HNM-2, which has  $\gamma$ +Laves formula and  $\gamma$ +Ni<sub>2</sub>(Nb, Ti, Mo) stoichiometry. This phase is brighter than that in 3GSA-HNM-2. It can demonstrate the presence of more amount of elements with large and heavy atoms in the phase. According to the EDS analysis (Figs. 4(d,e,f) and Table 6), it is understood that the phase is rich in Nb, Mo and Ti. The total amount of Nb and Mo for 3GSA-HNM-3 is 24.7%, whereas this amount is 21.8% for the same phase in the 3GSA-HNM-2. It is the reason for brighter color of phase in the 3GSA-HNM-3 in BSE mode. The total amount of Nb, Mo and Ti for phase *A*, and that of Ni, Co, Cr and Fe are 29.3% and 69.7%, respectively. These amounts fall within the Laves composition range. Thus, the  $\gamma$ +Laves intermetallic eutectic compounds have been formed in the 3GSA-HNM-3 on the basis of phase reactions (6) and (7).

It is interesting to say that the amount of Nb has increased in the  $\gamma$ +Laves intermetallic eutectic from 11.5% in the 3GSA-HNM-2 to 18% in 3GSA-HNM-3. Although the increasing amount of Nb to 1.3% in 3GSA-HNM-3 can be effective; however, it clarifies the high tendency of Nb for participation in the formation of Laves phase. Vice versa, Ti and Mo display a descending tendency in formation of Laves eutectic phase. In other words, Nb has absolute priority for the formation of Laves eutectic phase even if Ti and Mo are present.

Intermetallic phases with regular morphology are located just in the vicinity of  $\gamma$ +Laves intermetallic eutectic, which are specified by “*B*”. These phases are brighter than the matrix and darker than the Laves phase in BSE mode. The EDS analysis of this phase (Figs. 4(d, e, f) and Table 6) indicates that it is rich in Ni, Nb, Mo and Ti. The morphology and composition of such a phase have not been mentioned in earlier investigations. Based on the high content of Nb and Mo in this phase, it can be interpreted that some amount of Ti is replaced by these two heavy elements, and as a result, complex intermetallic Ni<sub>x</sub>(Ti,Nb,Mo) has been formed. According to the Ni–Ti and Ni–Nb equilibrium phase diagrams, it is found out that it directly nucleates from the molten metal, and probably it has solidified earlier (i.e., at higher temperatures), before the formation reaction of  $\gamma$ +Laves intermetallic eutectic begins. Therefore, it is a proeutectic phase and the relevant proeutectic phase reaction is as follows:



Moreover, “*C*” cubic precipitates with black color, which are surrounded by white  $\gamma$ +Laves intermetallic eutectics are dispersed within the microstructures (Fig. 4(c)). They have a clear semblance to the (Ti, Nb)(CN) constituents observed in the 3GSA-HNM-2. The significant segregation of Ti and Nb in the

interdendritic regions during the solidification has led to the precipitation of such complex carbonitrides in the solidified condition. “*D*” needle-like precipitates are seen around the  $\gamma$ +Laves intermetallic eutectics. They are bright in BSE mode. The EDS results display that they have more Nb than the austenite matrix (Figs. 4(d, e, f) and Table 6). They have grown by a specific crystallographic orientation in the segregation regions. Some researchers, who conducted their investigations on as-cast Nb-bearing Ni-based superalloys, have reported the formation of such an intermetallic phase that precipitates as Ni<sub>3</sub>Nb or  $\delta$  [19,26]. They are stable at the ambient temperature. These needle-shaped precipitates have nucleated and grown in the interdendritic regions. The time–temperature–transformation (TTT) diagram for alloy 718 indicates that  $\delta$  phase is formed within 700–1000 °C temperature range and is stable. The quantitative analysis shows that 10.3% Ni<sub>x</sub>(Ti,Nb,Mo) intermetallic phase with coarse plate morphology has been distributed in the microstructure (Figs. 1(c) and 4(b)). It is several times more than that observed in 3GSA-HNM-1 and -2. Indeed, the increasing Nb in the superalloy composition has facilitated Ti to produce more plate-like intermetallics. The simultaneous presence of high level of Ti and Nb in the superalloy composition stabilizes this phase. Unlike, decreasing Ti in the composition has caused the Laves to decrease from 6.1% in 3GSA-HNM-2, to 4.7% in 3GSA-HNM-3. Therefore, Ti can assist Nb in the formation of Laves eutectic intermetallics. On the other hand, some of Nb has been consumed by Ni<sub>x</sub>(Ti, Nb, Mo) intermetallic.

### 3.4 Intermetallics and secondary phases in microstructure of 3GSA-HNM-4

The microstructure of 3GSA-HNM-4 with the composition of  $\gamma$ -3.7%(Ti+Al) and 4.4% Nb is provided in Fig. 5. The nominal and dendritic core chemical compositions of the 3GSA-HNM-4 are presented in Table 8. In addition, the EDS spot microanalysis of the secondary phases is exhibited in Figs. 5(e,f). The composition of the related intermetallics and secondary phases has been collected in Table 8. The type, amount, morphology and distribution of the secondary phases within the 3GSA-HNM-4 microstructure are shown in Table 9.

Figure 5(a) displays the microstructure of 3GSA-HNM-4, which contains columnar dendrites with primary and secondary arms. The dendritic cores show a brighter color in comparison with the interdendritic regions. It appears that the interdendritic locations have corroded by the chemical etchant more severely than the other places, and therefore exhibit deeper level. It can be attributed to more susceptibility of interdendritic locations to corrosion. Figure 5(b) indicates the

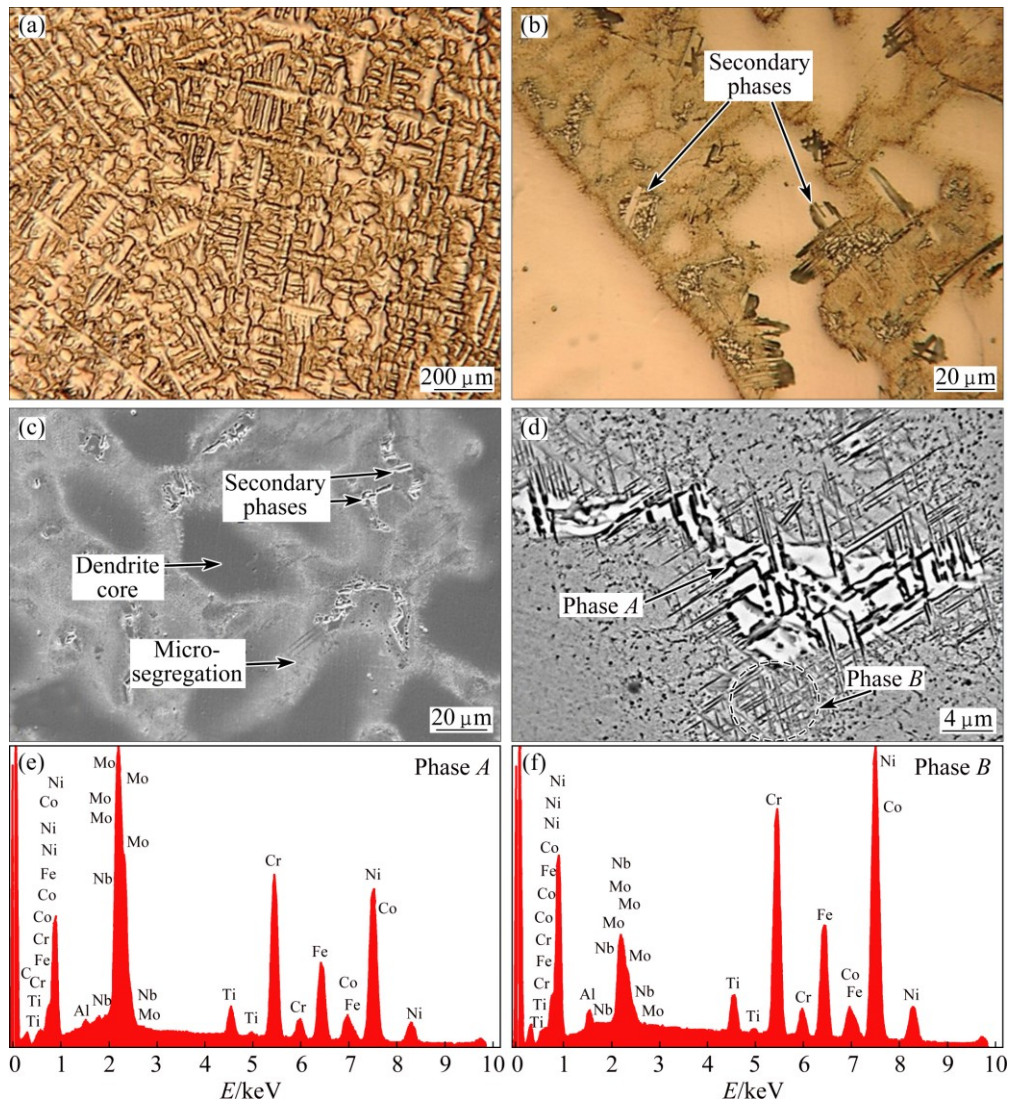


**Fig. 5** Microstructures of 3GSA-HNM-4: (a) Dendritic microstructure; (b) Micro-segregation and secondary phases in interdendritic regions; (c) Segregation and distribution of secondary phases in interdendritic regions in SE mode; (d) Segregation and distribution of secondary phases in BSE mode at higher magnification; (e, f) Related EDS microanalysis

**Table 8** Chemical analysis of dendritic cores and secondary phases in microstructure of 3GSA-HNM-4 (mass fraction, %)

Item	Ni	Co	Cr	Fe	Mo	Nb	Ti	Al
Alloy composition	52	3.8	18.8	13.9	3.5	4.4	2.6	1
Dendrite core	52.7	4.2	19.6	14.6	3.3	3	1.6	1
Phase A	39.4	4.1	14	9	6.2	22.4	4.6	0.3
Phase B	51	4.3	18.4	13.4	1.5	7.3	2.9	1.2

interdendritic locations, in which some secondary phases are formed. White phases and acicular precipitations are distributed there.

A significant microsegregation of alloying elements can be observed in Fig. 5(c). The secondary phases are nucleated among the segregation haloes. The compositional analysis carried out on the dendritic cores (see Table 8) demonstrates that Ti and Nb are severely

**Table 9** Type, amount, morphology, distribution of secondary phases and intermetallic eutectics in 3GSA-HNM-4 microstructure

No.	Phase transformation	Phase amount (surface)	Morphology	Distribution
1	$L \rightarrow \gamma$	Remained	Austenitic dendrites	All microstructures
2	$L \rightarrow \gamma + \text{Laves}$	6.6%	Lamellar intermetallic eutectics	Interdendritic regions
3	$\gamma \rightarrow \text{Ni}_3\text{Nb} \cdot \delta$	8.5%	Needle-like precipitates	Interdendritic regions

migrated from the cores and are rejected to the interdendritic regions. This situation can be detected for Mo with less severity. Figure 5(d) displays two types of secondary phases. The first is “A” layered white phases.

The composition of this phase based on Fig. 5(d) and Table 8, shows that it contains 22.4% Nb. The total amount of Nb, Ti and Mo in this phase reaches 33.2%. Therefore, according to the composition and the layered morphology of this phase, it can be concluded that the phase is  $\gamma$ +Laves intermetallic eutectic with  $Ni_2(Nb,Ti,Mo)$  stoichiometry. It has been formed in the 3GSA-HNM-4 on the basis of phase reactions (6) and (7). It is interesting to note that Nb content of the  $\gamma$ +Laves increases as Nb level of 3GSA-HNM-1 to -4 increases; while, Ti content of  $\gamma$ +Laves has a descending behavior in the 3GSA-HNM-1 to -4. These results reveal that Nb is the essential element for the formation of  $\gamma$ +Laves. In other words, this phase can be stabilized by Nb, even if Ti does not participate in it. Therefore, the absence of Nb in 3GSA-HNM-1 avoids the formation of  $\gamma$ +Laves in it. The presence of even low levels of Nb, as in the 3GSA-HNM-2, can promote the formation of  $\gamma$ +Laves in the microstructure. As seen in the 3GSA-HNM-2, the presence of 1.5% Nb, despite the presence of 7.6% (Ti+Al), can stop the formation of Ti/Al-rich  $\gamma+\gamma'$  intermetallic phase, instead, stabilize the  $\gamma$ +Laves intermetallic eutectic. Figure 5(d) exhibits white and needle-like precipitates “B”, which are formed in the vicinity of Laves eutectics and segregation regions. As discussed previously in 3GSA-HNM-3, they are  $Ni_3Nb:\delta$  intermetallics, which are formed during cooling of the alloy.

The phase measurements by the software showed that 6.6%  $\gamma$ +Laves has been formed (Fig. 1(d) and Fig. 5(c)). It is more than  $\gamma$ +Laves formed in the 3GSA-HNM-2 and -3. The noteworthy is the absence of  $\eta$ -Ni-Ti plate-shape intermetallics in the 3GSA-HNM-4. It demonstrates that decreasing Ti to less than 2.6% will lead to elimination of  $\eta$ -Ni-Ti intermetallics. Consequently, the released Nb from unformed  $\eta$ -Ni-Ti can promote the formation of more amount of  $\gamma$ +Laves intermetallics.

### 3.5 Correlation among composition, intermetallics and castability

The relation between the composition of superalloys and type-distribution of secondary phases is presented in Fig. 6. The relation among the composition and the type and amount of the secondary phases, which control the castability and weldability of the newly-designed superalloys, will assist the superalloy designing to optimize the composition and the consequent properties. In fact, the investigation of the current superalloys from type, amount, morphology and distribution of the intermetallic compounds from the microstructures viewpoint is due to their significant and governing influence on the next casting and welding operations. Based on Fig. 6, the diversity of the secondary phases

has decreased by decreasing the Ti+Al content of superalloys. The maximum amount of intermetallic eutectics (i.e., 41.5%) is formed in 9.8% (Ti+Al) content. New researches have been published and/or are under publishing by the author that evaluate the castability and weldability of the current superalloys [36,37]. It is anticipated that 3GSA-HNM-1 may show a remarkable susceptibility to hot cracking. In fact, high quantity of intermetallics formed in the 3GSA-HNM-1 can deteriorate its castability. The type and morphology of eutectic intermetallics change and the amount is considerably reduced by decreasing the Ti+Al content in 3GSA-HNM-2. Indeed, even a little quantity of Nb can easily destroy the stability of  $\gamma+\gamma'$ . Accordingly, it is predicted that the castability for the 3GSA-HNM-2 improves. This prediction can be conformed to the above mentioned references. The amount of Laves intermetallics shows an ascending behavior again, however with less intensity, by increasing the Nb content in the 3GSA-HNM-3. The same trend is seen for 3GSA-HNM 4. It means that by increasing the Nb to 4.4%, and decreasing the Ti+Al to 3.7% in 3GSA-HNM-4, the amount of Laves intermetallics augments. Therefore, it is predicted that castability weakens again in 3GSA-HNM-4. Finally, it is anticipated that the best castability is obtained for 3GSA-HNM-3 with composition of  $\gamma$ -5.7%(Ti+Al) and 2.9% Nb. It is due to the formation of minimum amount of eutectic intermetallics (i.e., 4.7%), which has the most effects on the castability.

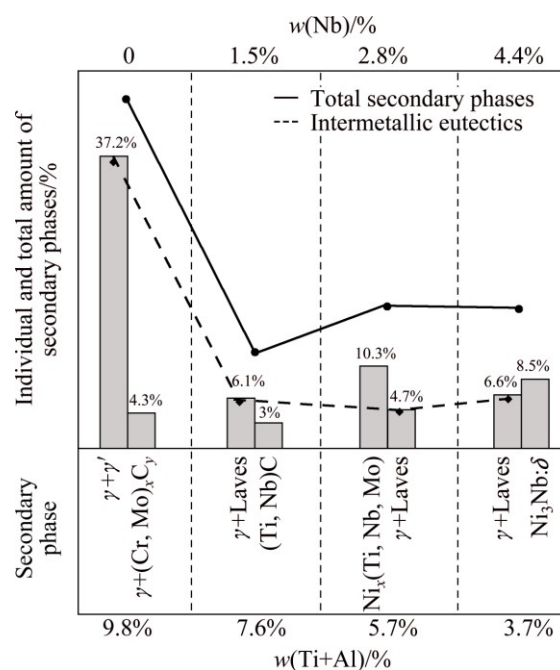


**Fig. 6** Relation between composition of superalloys and type, distribution and amount of secondary phases (The spheres show total amount of volume fraction of secondary phases in each superalloy)

## 4 Conclusions

1) The maximum amount of intermetallic eutectics (i.e., 41.5%) has been formed in 9.8% (Ti+Al) content. High level of intermetallics formed in the 3GSA-HNM-1 deteriorates its castability.

2) The type and morphology of eutectic intermetallics change and the amount is considerably reduced by decreasing the Ti+Al content in 3GSA-HNM-2. Even a little amount of Nb can easily destruct the stability of  $\gamma+\gamma'$ . It is predicted that the castability for the 3GSA-HNM-2 improves.

3) By increasing the Nb content to 4.4% and decreasing the Ti+Al content to 3.7% in 3GSA-HNM-4, the amount of Laves intermetallics increases. The castability is anticipated to weaken in 3GSA-HNM-4.

4) It is anticipated that the best castability is obtained for 3GSA-HNM-3 with the composition of  $\gamma$ -5.7%(Ti+Al) and 2.9% Nb. It is due to the formation of minimum amount of eutectic intermetallics (i.e., 4.7%) in the microstructure.

## Acknowledgment

The author likes to thank the academic stuff of Meccanica Dipartimento Politecnico di Milano University, Milano, Italy, professor Carlo Mapelli, Dr. Silvia Barella, Dr. Davide Mombelli and Dr. Andrea Gruttadauria for their laboratory facilities and kind cooperation.

## References

- [1] REED R C. The superalloys fundamentals and applications [M]. Cambridge University Press, 2006.
- [2] DUPONT J, LIPOLD J, KISER S. Welding metallurgy and weldability of nickel-base alloys [M]. Wiley and Sons Inc, 2009.
- [3] LACHOWICZ M, DUDZIŃSKI W, HAIMANN K, PODREZ-RADZISZEWSKA M. Microstructure transformations and cracking in the matrix of  $\gamma-\gamma'$  superalloy inconel 713C melted with electron beam [J]. Materials Science Engineering A, 2008, 479: 269–276.
- [4] ZHAO S, XIE X, SMITH G D, PATEL S J. Microstructural stability and mechanical properties of a new nickel-based superalloy [J]. Materials Science and Engineering A, 2003, 355: 96–105.
- [5] ATTALLAH M M, TERASAKI H, MOAT R J, BRAY S E, KOMIZO Y, PREUSS M. In-situ observation of primary  $\gamma'$  melting in Ni-base superalloy using confocal laser scanning microscopy [J]. Materials Characterization, 2011, 62: 760–767.
- [6] METZLER D A. A gleeble-based method for ranking the strain-age cracking susceptibility of Ni-based superalloys [J]. Welding Journal, 2008, 87: 249–256.
- [7] THOMPSON R G, DOBBS J R, MAYO D E. The effect of heat treatment on microfissuring in Alloy 718 [J]. Welding Journal, 1986: 299–304.
- [8] DAVIES G J. Solidification and casting [M]. Applied Science Publisher Ltd, 1973.
- [9] ASM Metal Handbook: Casting [M]. ASM International, 1992.
- [10] WILSON B C, CUTLER E R, FUCHS G E. Effect of solidification parameters on the microstructures, and properties of CMSX-10 [J]. Materials Science and Engineering A, 2008, 479: 356–364.
- [11] CAMPBELL J. Stop pouring, start casting [C]//AFS Proceedings. Schaumburg, USA: American Foundry Society, 2012: 1–11.
- [12] EGBEWANDE A T, BUCKSON R A, OJO O A. Analysis of laser beam weldability of Inconel 738 superalloy [J]. Materials Characterization, 2010, 61: 569–574.
- [13] CHIANG M F, CHEN C. Induction-assisted laser welding of IN-738 nickel-base superalloy [J]. Materials Chemistry and Physics, 2009, 114: 415–419.
- [14] ÖSTERLE W, KRAUSE S, MOELDERS T, NEIDEL A, ODER G, VÖLKER J. Influence of heat treatment on microstructure and hot crack susceptibility of laser-drilled turbine blades made from René 80 [J]. Materials Characterization, 2008, 59: 1564–1571.
- [15] RUSH M T, COLEGROVE P A, ZHANG Z, BROAD D. Liquation and post-weld heat treatment cracking in Rene 80 laser repair welds [J]. Journal of Materials Processing Technology, 2012, 212: 188–197.
- [16] DUPONT J N, ROBINO C V, MICHAEL J R, NOTIS M R, MARDER A R. Solidification of Nb-bearing superalloys: Part I. Reaction sequences [J]. Metallurgical and Materials Transitions A, 1998, 29: 2785–2796.
- [17] RADHAKRISHNAN B, THOMPSON R G. Liquid film migration (LFM) in the weld heat-affected zone (HAZ) of a Ni-base superalloy [J]. Scripta Metallurgica, 1990, 24: 537–542.
- [18] THOMPSON R G, CASSIMUS J J, MAYO D E, DOBBS J R. The relationship between grain size and microfissuring in Alloy 718 [J]. Welding Journal, 1985: 91–96.
- [19] BAESLACK W A, NELSON D E. Morphology of weld heat-affected zone liquation in cast Alloy 718 [J]. Metallography, 1986, 19: 371–379.
- [20] CAO X, RIVAUX B, JAHAZI M, CUDDY J, BIRUR A. Effect of pre- and post-weld heat treatment on metallurgical and tensile properties of Inconel 718 alloy butt joints welded using 4 kW Nd:YAG laser [J]. Journal of Materials Science, 2009, 44: 4557–4571.
- [21] ODABAS A, ÜNLÜİ N, GÖLLER G, ERUSLU M I. A study on laser beam welding (LBW) technique: effect of heat input on the microstructural evolution of superalloy Inconel 718 [J]. Metallurgical and Materials Transitions A, 2010, 41: 2357–2365.
- [22] REDDY G M, MURTHY C V S, RAO K S, RAO K P. Improvement of mechanical properties of Inconel 718 electron beam welds—Influence of welding techniques and post weld heat treatment [J]. International Journal of Advanced Manufacturing Technology, 2009, 43: 671–680.
- [23] SIVARPASAD K, SUNDARARAMAN S G. Influence of weld cooling rate on microstructure and mechanical properties of alloy 718 weldments [J]. Metallurgical and Materials Transitions A, 2008, 39: 2115–2127.
- [24] VISHWAKARMA K R, RICHARDS N L, CHATURVEDI M C. Microstructural analysis of fusion and heat-affected zones in electron beam welded ALLVAC® 718PLUSTM superalloy [J]. Materials Science and Engineering A, 2008, 480: 517–528.
- [25] KRENZ D, EGBEWANDE A T, ZHANG H R, OJO O A. Single pass laser joining of Inconel 718 superalloy with filler [J]. Materials Science and Technology, 2011, 27: 268–274.
- [26] QIAN M, LIPPOLD J C. The effect of annealing twin-generated special grain boundaries on HAZ liquation cracking of nickel-base superalloys [J]. Acta Materialia, 2003, 51: 3351–3361.
- [27] QIAN M, LIPPOLD J C. The effect of rejuvenation heat treatments on the repair weldability of wrought alloy 718 [J]. Materials Science and Engineering A, 2003, 340: 225–231.
- [28] ZHANG H R, OJO O A. Non-equilibrium liquid phase dissolution of  $\delta$  phase precipitates in a nickel-based superalloy [J]. Philosophical

- Magazine Letter, 2009, 89: 787–794.
- [29] HUANG C A, WANG T H, LEE C H, HAN W C. A study of the heat-affected zone (HAZ) of an Inconel 718 sheet welded with electron-beam welding (EBW) [J]. *Materials Science and Engineering A*, 2005, 398: 275–281.
- [30] LONG Y T, NIE P L, LI Z G, HUANG J, LI X, XU X M. Segregation of niobium in laser cladding Inconel 718 superalloy [J]. *Transactions of Nonferrous Metals Society of China*, 2016, 26: 431–436.
- [31] OJO O A, RICHARDS N L, CHATURVEDI M C. Contribution of constitutional liquation of gamma prime precipitate to weld HAZ cracking of cast Inconel 738 superalloy [J]. *Scripta Materialia*, 2004, 50: 641–646.
- [32] MONTAZERI M, GHAINI F M. The liquation cracking behavior of IN738LC superalloy during low power Nd:YAG pulsed laser welding [J]. *Materials Characterization*, 2012, 67: 65–73.
- [33] FERRO P, ZAMBON A, BONOLLO F. Investigation of electron-beam welding in wrought Inconel 706—Experimental and numerical analysis [J]. *Materials Science and Engineering A*, 2005, 392: 94–105.
- [34] DUDZIŃSKI M L W, RADZISZEWSKA M P. TEM observation of the heat-affected zone in electron beam welded superalloy Inconel 713C [J]. *Materials Characterization*, 2008, 59: 65–73.
- [35] SIDHU R K, OJO O A, CHATURVEDI M C. Microstructural analysis of laser-beam-welded directionally solidified INCONEL 738 [J]. *Metallurgical and Materials Transactions A*, 2007, 38: 858–870.
- [36] NAFFAKH MOOSAVY H, ABOUTALEBI M R, SEYEDEIN S H, MAPELLI C. A Solidification model for prediction of castability in the precipitation-strengthened nickel-based superalloys [J]. *Journal of Materials Processing Technology*, 2013, 213: 1875–1884.
- [37] NAFFAKH MOOSAVY H, ABOUTALEBI M R, SEYEDEIN S H. An analytical algorithm to predict weldability of precipitation-strengthened nickel-base superalloys [J]. *Journal of Materials Processing Technology*, 2012, 212: 2210–2218.

## 含 Ti/Al/Nb 镍基高温合金的 显微组织及可铸造能力预测

Homam NAFFAKH-MOOSAVY

Department of Materials Engineering, Faculty of Engineering,  
Tarbiat Modares University, P. O. Box 14115-143, Tehran, Iran

**摘要:** 对第三代镍基高温合金中  $\gamma/\gamma'$  和  $\gamma/\text{Laves}$  金属间化合物随合金中 Ti、Al、Nb 含量的变化的定量关系进行研究。结果表明, 当合金(3GSA-HNM-1 合金)含 9.8%(质量分数)(Ti+Al)时, 其生成的共晶化合物含量最高可达 41.5%, 这种高含量的共晶化合物会导致合金的铸造能力降低。对 3GSA-HNM-2 合金(含  $\gamma$ -7.6%(Ti+Al)和 1.5%Nb), 随(Ti+Al)含量的降低, 生成的共晶化合物种类和形貌均发生了变化, 数量也显著减少, 可预计其铸造能力会得到改善。对 3GSA-HNM-3 合金(含  $\gamma$ -5.7%(Ti+Al)), 随着 Nb 含量的增加, 生成的 Laves 相数量减少, 虽然程度有所降低。因此, 对含 2.9% Nb 的 3GSA-HNM-3 合金( $\gamma$ -5.7%(Ti+Al)), 由于生成的共晶化合物数量最少(4.7%), 其可铸造能力最好。

**关键词:** 镍基高温合金; 第二相; 可铸造能力; 偏析; 显微组织

(Edited by Sai-qian YUAN)